iScience

CellPress
OPEN ACCESS

Article

Condensation of water vapor from humid air inside vertical channels formed by flat plates

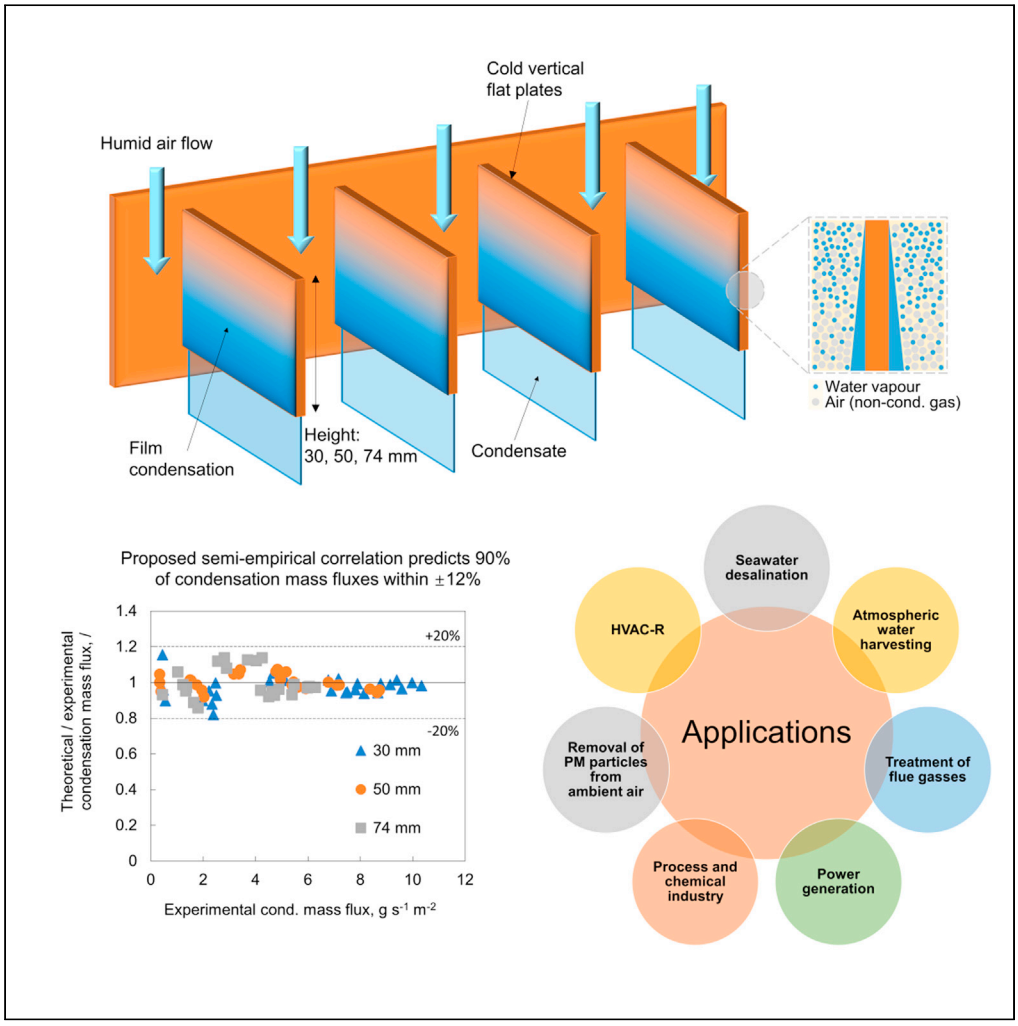

Primož Poredoš, Nada Petelin, Boris Vidrih, Tilen Žel, Qiuming Ma, Ruzhu Wang, Andrej Kitanovski

rzwang@sjtu.edu.cn (R.W.)
andrej.kitanovski@fs.uni-lj.si (A.K.)

Highlights

Experimental and theoretical study of humid air condensation on vertical plates

Unique condenser geometry was proposed, allowing re-use of condensation latent heat

A new correlation for humid air condensation on a series of plates was proposed

Potential application of correlation for fresh water generation was demonstrated

Poredoš et al., iScience 25, 103565
January 21, 2022
https://doi.org/10.1016/j.isci.2021.103565

iScience

CellPress
OPEN ACCESS

Article

Condensation of water vapor from humid air inside vertical channels formed by flat plates

Primož Poredoš,[1,2] Nada Petelin,[2] Boris Vidrih,[2] Tilen Žel,[2] Qiuming Ma,[1] Ruzhu Wang,[1,*] and Andrej Kitanovski[2,3,*]

SUMMARY

Condensation of humid air is an important process in thermal and process engineering and a subject of many currently research-intensive scientific domains, such as atmospheric water harvesting and seawater desalination. The nature of (water) vapor condensation in the presence of non-condensable gas (NCG) such as air differs significantly from the case with the pure, quiescent vapor condensation. In the literature, simple models that describe the forced flow condensation of water vapor in the presence of air on a series of vertical flat plates are hard to find. Here we present a simple and computationally efficient semi-empirical correlation describing forced flow condensation from humid air inside vertical channels formed by flat plates. The correlation accounts air as a non-condensing gas, different heights of vertical plates, and different thermal-hydraulic parameters. The correlation has been experimentally validated and shows excellent agreement, as 90% of theoretically predicted values are within ±12% of experimental data.

INTRODUCTION

Condensation process plays an important role in several engineering applications and processes, spanning from power generation (Uchida et al., 1965), advanced treatment of desulfurized flue gasses (Cao et al., 2021), removal of PM particles from ambient air (Xu et al., 2017), refrigeration and air conditioning (Wang et al., 2018), and process industry (Chen et al., 2020) to emerging research areas, such as seawater desalination (Ma et al., 2021; Zanganeh et al., 2020; Zhang et al., 2021) and atmospheric water harvesting (AWH) (Ejeian and Wang, 2021; Wang et al., 2021), and is becoming more important in the booming field of daytime radiative cooling (Farooq et al., 2021; Haechler et al., 2021; Trosseille et al., 2021).

A theory of the film condensation in the case of pure quiescent vapor condensation on a vertical flat surface was analytically solved by Nusselt in 1916 (Nusselt, 1916). The derived equation that allows the calculation of the Nusselt number for that case with several assumptions is well known (Nusselt, 1916). However, when the vapor contains two or more species, for instance, in the case of the gaseous mixture of water and air representing humid air, only water vapor condenses. The air as a non-condensing gas (NCG) does not condense. Owing to water vapor diffusion into the liquid condensate (thereby $W_{2,i} < W_{2,b}$), the mass fraction of air increases near the liquid-vapor interface ($W_{1,i} > W_{1,b}$), as shown in Figure 1, Details A and B. According to the phase rule, the temperature of the mixture decreases from the bulk temperature $T_{a,b}$ (corresponding to the bulk flow humid air temperature) to the temperature at the liquid-vapor interface $T_{a,i}$ (Fujii, 1991), which is schematically shown in the Figure 1, Detail B. The reduction of the water vapor saturation temperature at the interface due to the presence of the air leads to the reduction of the condensation heat transfer and mass flow rates in comparison with the case with the pure water vapor condensation with the same cooling surface (T_w) and bulk flow temperatures ($T_{a,b}$).

The influence of NCG on condensation has been experimentally confirmed in 1929 by Othmer (Othmer, 1929). When the volume fraction of air in steam-air mixture increased from 0% to 0.5%, the condensation heat transfer coefficient reduced by nearly 50%. More recently, the influence of air on condensation was experimentally studied by Bum-Jin et al. (2004). A large detrimental effect on heat transfer rate was demonstrated in the case of small air mass concentrations (1.6%–6.5%). For the drop-wise condensation,

[1]Institute of Refrigeration and Cryogenics, Engineering Research Center of Solar Power and Refrigeration (MOE China), Shanghai Jiao Tong University, 800 Dongchuan Road, Shanghai 200240, China

[2]Laboratory for Refrigeration and District Energy, University of Ljubljana, Faculty of Mechanical Engineering, Aškerčeva cesta 6, 1000 Ljubljana, Slovenia

[3]Lead contact

*Correspondence: rzwang@sjtu.edu.cn (R.W.), andrej.kitanovski@fs.uni-lj.si (A.K.)

https://doi.org/10.1016/j.isci.2021.103565

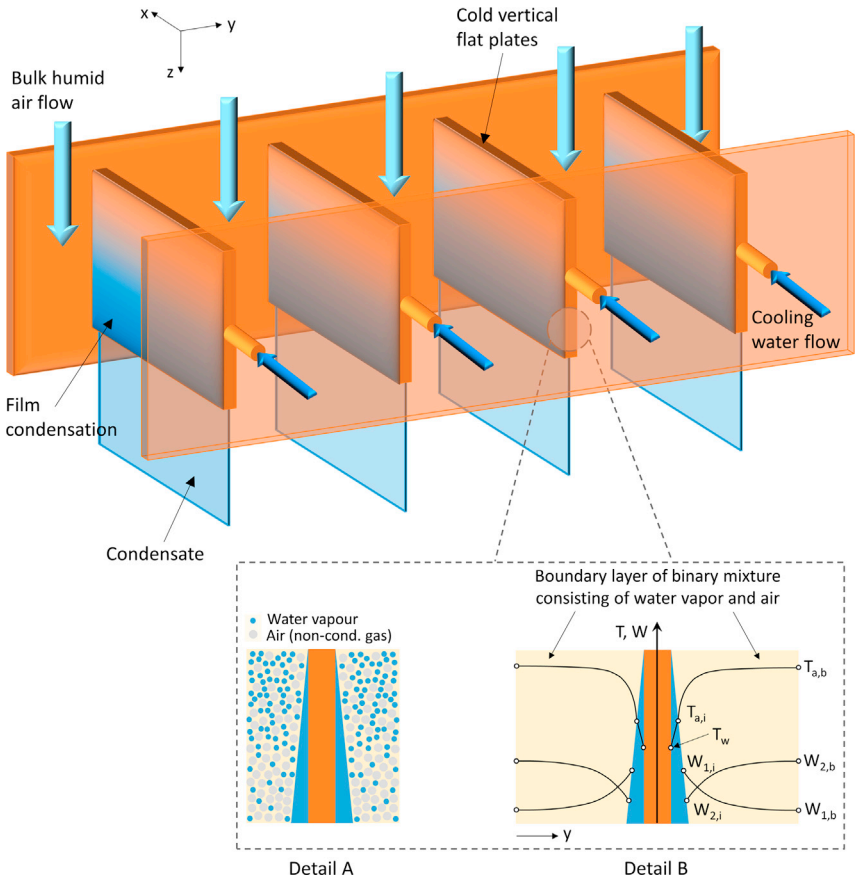

Figure 1. Condensation of water vapor in the presence of air as a non-condensing gas

Condensation of water vapor (index 2 in Detail B) in the presence of air as a non-condensing gas (index 1 in Detail B) during the humid air flow over cold vertical flat plates forming vertical channels.

significantly higher heat flux reductions were observed in comparison with the film-wise. The condensation heat transfer reduction was confirmed also with the presence of other NCG. Ge et al. (2016) experimentally investigated convection film condensation of steam in the presence of CO_2 on a vertical plate. The increase of CO_2 mass fraction from 23.3% to 74.8% led to a significant reduction in heat flux (by about five times).

Aside from experimental studies, the condensation process in the presence of NCG has also been extensively theoretically studied by researchers. The developed theoretical models span from simple semi-empirical correlations (Asano et al., 1979; Corradini, 1984; Fujii, 1991; Kim and Corradini, 1990; Liao and Vierow, 2006) to complex and computationally extensive numerical models (Charef et al., 2017; Ganguli et al., 2008; Karkoszka, 2007; Li and Li, 2011; Naylor and Friedman, 2010; Saraireh et al., 2010; Siow et al., 2002, 2004, 2007; Yi et al., 2015). Simple models provide relatively accurate results within the applicable ranges, defined by their corresponding theoretical and experimental study. In the case of more complex geometries, physical models, and operating conditions, numerical models can be applied, where fully resolved numerical simulations of a fluid flow are required. This leads to increased computational time and costs and inherently increases overall model complexity. The main drawback of complex numerical models is the limited application range, typically valid for specific geometry-based case.

The simplest known semi-empirical correlations that consider NCG have been reported by Uchida and Tagami in 1965 (Tagami, 1965; Uchida et al., 1965). Both correlations (Uchida: $h_{Uchida} = 379(m_{air}/m_{steam})^{-0.707}$ [W m^{-2} K^{-1}], for $m_{air}/m_{steam} < 20$; Tagami: $h_{Tagami} = 11.4 + 284(m_{steam}/m_{air})$ [W m^{-2} K^{-1}], for $0 < m_{steam}/m_{air} < 1.4$) are based on steady-state data and were correlated as a function of only the air to steam mass ratio. The developed correlations were used extensively in nuclear industry, particularly for the light water reactor (LWR) licensing calculations (Corradini, 1984). As research activities related to the safety of

LWR intensified, Corradini (1984) and Kim et al. (Kim and Corradini, 1990) proposed models based on the stagnant film model. Their models predicted the condensation rates in the presence of an NCG in a reactor containment and were in good agreement with the experimental data. An alternative model, based on generalized diffusion layer approach has been proposed by Liao et al. (Liao and Vierow, 2006). The new model improves the existing diffusion layer model (Peterson et al., 1992) by expressing the Fick's law of diffusion on a mass basis rather on a molar basis. A thorough theoretical analysis for the case of film condensation of binary and multi-component vapors containing NCG on vertical plate has been published by Fujii (1991). This was achieved by solving the equations of the two-phase boundary layer theory with the use of the similarity transformation. The same method has been applied by Asano et al. (1979), who investigated forced convection film condensation of different vapors (water vapor, methanol, benzene, and carbon tetrachloride) on vertical plate in the presence of air. Relatively good agreement between experimental data and theoretical model has been observed, as deviations were smaller than 30%.

A rather complex mathematical model, built upon the boundary layer equations that were transformed with nondimensional coordinates and solved using finite difference method, was presented by Cheng et al. (Li and Li, 2011). Naylor et al. (Naylor and Friedman, 2010) analyzed the laminar film condensation on a vertical flat plate in a crossflow of humid air using an approximate numerical method. Karkozska (2007) investigated forced and free convection condensation of water vapor in the presence of air (binary) and air with helium (ternary mixture) on vertical and horizontal plates. This was done theoretically by using a similarity method and computational fluid dynamics. Ganguli et al. (2008) developed a theoretical model for free convection film condensation of steam on a vertical flat plate in the presence of air and helium for both laminar and turbulent regimes. This model was based on diffusion layer theory and numerically solved using an iterative procedure. For the case of both laminar and turbulent regimes, Yi et al. (2015) presented numerical simulation using the Volume of Fluid model of the humid air film condensation on vertical plate for inlet air mass fractions in the range 5%–50%. All authors reported reasonable agreement with existing numerical and/or experimental data.

In some cases, pairs of vertical plates represent vertical channels with the humid air flowing in between. The Nusselt numbers for convection film condensation of pure vapors in such cases can be easily obtained (Kakac et al., 1987; Roetzel et al., 2019). For the case of multi-component vapors containing NCG, Siow et al. (2002, 2004, 2007) investigated film condensation of steam-air mixtures for horizontal, vertical, and inclined channels. A numerical model was provided by solving boundary-layer equations using a fully coupled implicit numerical approach. A similar study was performed by Charef et al. (2017) for laminar film condensation of humid air along an inclined channel, where boundary layer equations were solved using the implicit finite difference method. By using the finite control volume approach, Ait Hssain provided a numerical solution of laminar convective condensation in the presence of NCG in the case of downward flowing humid air (Ait Hssain et al., 2019). Besides, the author also investigated the influence of copper nanoparticles presence on the condensation performance (Ait Hssain et al., 2021). Saraireh et al., 2010 modeled laminar and turbulent film condensation of pure steam and air-steam mixture flow in a vertical channel. The obtained differential equations were discretized using finite difference approach and solved using the fourth-order Runge-Kutta method. Obtained solutions showed satisfactory agreement with the presented experimental data.

Upon a comprehensive literature study, we observed lack of simple models related to humid air flow over a series of vertical flat plates forming vertical channels. Several complex models describing the condensation of humid air on vertical plates do exist but are predominantly computationally demanding (Charef et al., 2017; Ganguli et al., 2008; Karkoszka, 2007; Li and Li, 2011; Naylor and Friedman, 2010; Saraireh et al., 2010; Siow et al., 2002, 2004, 2007; Yi et al., 2015). Moreover, there is no study, either theoretical or experimental, related to the condensation of water vapor in presence of air on a series of vertical flat plates that form hollow channels. Recently a paper related to the condensation of humid air on vertical flat plates with the height of 74 mm and on horizontal tubes with the outer diameters of 15 and 40 mm has been published (Poredoš et al., 2021b). The main goal was to evaluate existing semi-empirical correlations from the literature and to provide the corrected empirical coefficients using the power regression data analysis based on experimental values. As the study was of applicable nature with the aim to provide simple correlations to support the tumble dryer's condensation geometry evaluation, the theoretical insight into the condensation process and the correlation development was limited.

Herein, we present an in-depth theoretical and experimental study that considers water vapor condensation in the presence of air as a non-condensable gas on a series of vertical flat plates forming vertical channels, as is schematically shown in Figure 1. The focus of this study was to comprehensively investigate the condensation process

on vertical flat plates forming vertical channels, emphasized with the following unique features: (1) The designed condensation test sections consist of vertical flat plates with three different heights (30, 50, and 74 mm) that form hollow vertical channels. Inside the channels a cooling water provides cooled condensation surface at nearly isothermal conditions. The proposed design of the test section therefore allows harnessing of the condensation latent heat, released during the water vapor condensation. In addition, owing to the geometry of the proposed test sections we evaluated the condensation on its side walls. (2) We discuss the importance of the humid air flow classification inside the vertical channels. Our analysis of velocity, thermal and concentration boundary layers thicknesses versus inter-channel dimensions provides a crucial design consideration, which defines either internal or external fluid flow exists within the channel. (3) The presented semi-empirical correlation, based on external humid air flow assumption is computationally efficient, easy to implement in computer program and has been experimentally validated, showing excellent agreement between calculated and experimental values. Here we note that the presented correlation is not valid for condenser geometries with densely packed vertical plates but is valid only for condenser geometries where the distance between the plates is larger from the point of view of boundary layer existence. (4) The study focused on characteristics of condensation heat transfer with respect to different heights of vertical flat plates and thermal-hydraulic parameters. (5) The applicability and the usability of the new semi-empirical correlation is demonstrated by evaluation of the potential condenser performance during the fresh water generation (seawater desalination and adsorption-based atmospheric water harvesting).

RESULTS

The development of a new semi-empirical correlation

The presented new semi-empirical correlation separately considers (1) the condensate flow, which accounts the shear stress at the liquid-vapor interface; (2) bulk flow of humid air as a laminar flow of a fluid over an isothermal plate neglecting viscous dissipation in the bulk flow; and (3) the account of the non-condensable component in the bulk flow. The correlation, valid for the calculation of the water vapor condensation in the presence of air on a series of vertical flat plates forming vertical channels has been made with the following assumptions:

1. Film condensation on vertical plates.
2. The entire condensing surface is covered by condensate; hence a completely wet copper surface is assumed and no condensate movement in the form of rivulets exists. This assumption is backed up by the typical equilibrium contact angle of a water droplet on a copper surface in the presence of air at 20°C to be ~60–70° (Chougule and Sahu, 2016; Martinez-Urrutia et al., 2018). Furthermore, as the water surface tension decreases with increasing water temperature, so does the contact angle (Song and Fan, 2021).
3. The condensate film thickness is significantly smaller compared with the distance between two neighboring vertical plates forming a vertical channel and the width of the plate.
4. The distance between two neighboring vertical plates forming a vertical channel is significantly larger compared with the velocity, thermal and concentration boundary layer thicknesses (see STAR Methods and Figure S4). Therefore, the external flow of humid air over a flat vertical plate has been considered.
5. The wall temperature is assumed to be constant over the entire height and width of the vertical plate.
6. Homogeneous process parameters (temperature, velocity, and water vapor mass fraction) of the humid air at the test section inlet cross section.
7. The density of the condensate is significantly larger compared with the density of the humid air.
8. Shear stress at the liquid-gas interface is equal to the wall shear stress.
9. Heat losses to the ambient are disregarded.

The film condensation assumption is backed up by the fact that a small amount of condensate on the plate spurs film condensation (Fujii, 1991), where $\sim 10^{-1}$ mm is listed as a typical order of magnitude of film thickness.

Condensate mass flux calculation

The detailed presentation of the new semi-empirical correlation development along a nomenclature is presented in STAR methods.

The mass conservation in the case of the condensation process is always assumed, as no mass is produced or destroyed. Hence, the condensate mass flux can be calculated by knowing the mass flux of a water vapor diffusing into condensate (Stephan and Laesecke, 1980), also considering the correction factor F accounting the air as a non-condensable gas (see STAR Methods):

$$n''_{2,x} = \rho_{a,i}\, \beta_{2,x}\, F \qquad \text{(Equation 1)}$$

where $\beta_{2,x}$ is a local mass transfer coefficient and $\rho_{a,i}$ is the density of humid air at the interface. The mass transfer coefficient is related to the Sherwood number by the following relation: $Sh = \beta x/D$. Inserting this equation into Equation 1, integrating $n''_{2,x}$ with respect to x from 0 to L, also considering Equations 25 and 27 from STAR Methods, the condensate mass flow rate per unit height of plate can be obtained as:

$$\Gamma(L) = \int_0^L n''_{2,x}dx = 0.604\rho_{a,i}D_{2-1,i}\left(\frac{2.5}{1.5+\frac{W_{1,i}}{W_{1,b}}}\right)^m \left(\frac{W_{1,i}-W_{1,b}}{W_{1,b}}\right)^{0.931} Sc_{a,i}^{1/3} Re_{a,b}^{1/2} \qquad \text{(Equation 2)}$$

Within Equation 2, $D_{2\text{-}1,i}$ is the mass diffusivity of water vapor in air and $Sc_{a,i}$ is the Schmidt number of humid air. Both variables are defined at the liquid-gas interface temperature. The Schmidt number at the interface was calculated as:

$$Sc_{a,i} = \frac{\mu_{a,i}}{\rho_{a,i}D_{2-1,i}} \qquad \text{(Equation 3)}$$

where $\mu_{a,i}$ is dynamic viscosity of the humid air at the interface. Mass diffusivity of water vapor in air at the interface was determined according to the empirical correlation, as proposed by Fuller (1966):

$$D_{2-1,i} = \frac{10^{-3}T_{a,i}^{1.75}(1/\tilde{M}_1 + 1/\tilde{M}_2)^{1/2}}{p_{tot}\left[V_1^{1/3}+V_2^{1/3}\right]^2} \qquad \text{(Equation 4)}$$

where $\tilde{M}_1$ and $\tilde{M}_2$ are molar masses of air and water, respectively, whereas V_1 and V_2 represent atomic diffusion volumes of air and water, respectively. Finally, the theoretical condensate mass flux can be calculated using the following equation:

$$\Gamma(L) = m''_{avg,th}\, L \qquad \text{(Equation 5)}$$

One of the most important parameters that is difficult to obtain through experiments is the temperature at the liquid-gas interface, T_i. The calculation of T_i starts with the assumption of temperature equality between interface and the wall, i.e., $T_w = T_i$. However, as the $T_i > T_w$ is always true, later iterations of the calculation are based on the following equation: $T_i = T_w + (T_i - T_w)_{avg,new}$.

Using Equation 21 from STAR Methods, and knowing that $d\Gamma(L)/dx = n''_{2,x}$, the temperature difference can be expressed as:

$$(T_i - T_w)(x) = \frac{h_{fg}n''_{2,x}\delta}{k_c} \qquad \text{(Equation 6)}$$

The condensate thickness δ can be calculated combining Equation 19 from STAR Methods and Equation 2, where the second term in Equation 19 can be omitted. This step has been justified by comparing the left and right parts of Equation 19. Before that, we also determined the order of magnitude of a shear stress at the interface for a plate height 0.05 m according to the Equation 23 from STAR Methods. With the average value of experimentally determined velocity of the humid air ≅ 1m s^{-1}, it follows $U_{a,b}^{3/2} \sim 10^0$, whereas the order of magnitudes of the humid air density and viscosity are 10^0 and 10^{-5}, respectively. The order of magnitude of the shear stress at the interface is therefore 10^{-2}. Using this approximate number denoting shear stress on the right-hand side of Equation 19 and also by knowing the order of magnitude of the following variables: $g \sim 10^1$, $\rho_c \sim 10^3$, $\delta \sim 10^{-4}$, $\mu_c \sim 10^{-3}$, the approximate values of left and right sides of Equation 19 are $\Gamma \cong 10^{-3} + 10^{-8}$. Consequently, the condensate thickness has the following equation:

$$\delta = 1.26\left(\frac{\mu_c\rho_{a,i}D_{2-1,i}}{g\rho_c^2}\right)^{\frac{1}{3}} Sc_{a,i}^{1/9} Re_{a,b}^{1/6} F^{\frac{1}{3}} \qquad \text{(Equation 7)}$$

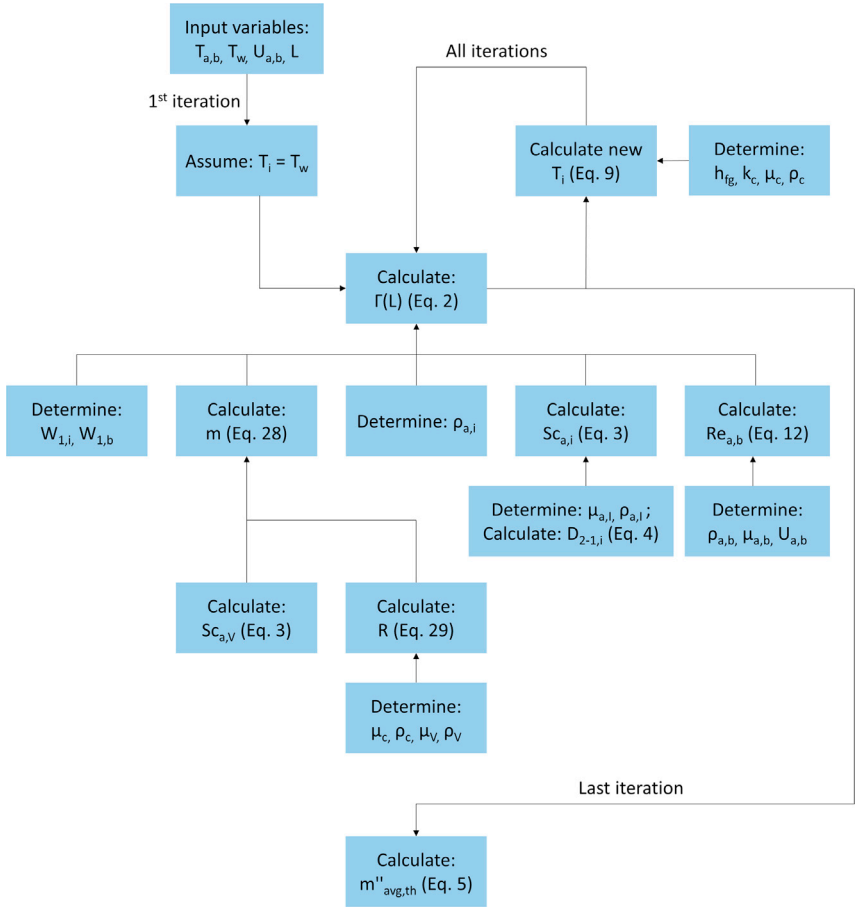

Figure 2. Flowchart of the condensate mass flux calculation procedure

To calculate the average temperature difference $(T_i - T_w)_{avg,new}$, we integrated Equation 6 with respect to x from 0 to L. If we also divide by L, the final form of the equation is then:

$$(T_i - T_w)_{avg,new} = \frac{3}{2}\left(\frac{0.418\rho_{a,i}D_{2-1,i}h_{fg}}{k_c}\right)\left(\frac{\mu_c\rho_{a,i}D_{2-1,i}}{g\rho_c^2L^3}\right)^{1/3} Sc_{a,i}^{4/9}Re_{a,b}^{2/3}F^{4/3} \quad \text{(Equation 8)}$$

By considering Equation 2, Equation 8 can be also expressed as:

$$(T_i - T_w)_{avg,new} \cong 1.082\left(\frac{h_{fg}}{k_c}\right)\left(\frac{\mu_c}{g\rho_c^2L^3}\right)^{1/3}\Gamma(L)^{4/3} \quad \text{(Equation 9)}$$

Variables defined in Equation 8 are dependent on the temperature at the interface T_i. This equation is solved iteratively, where first we assume $T_i = T_w$ and the first value of $(T_i - T_w)_{avg,new}$ is obtained. Then, new temperature T_i can be calculated and used to solve Equation 8. This procedure is repeated until the convergence is obtained, which in our case is up to 10 iterations. The properties of the condensate (k_c, μ_c, and ρ_c) were evaluated at the reference temperature T_c, as defined by Denny et al. (Denny and Mills, 1969):

$$T_c = T_w + \frac{1}{3}(T_i - T_w) \quad \text{(Equation 10)}$$

To reduce the complexity of the condensate mass flux calculation based on the described semi-empirical correlation, the entire process of the condensate mass flux calculation is shown in Figure 2. Variables that need to be either calculated or determined are highlighted within blue squares.

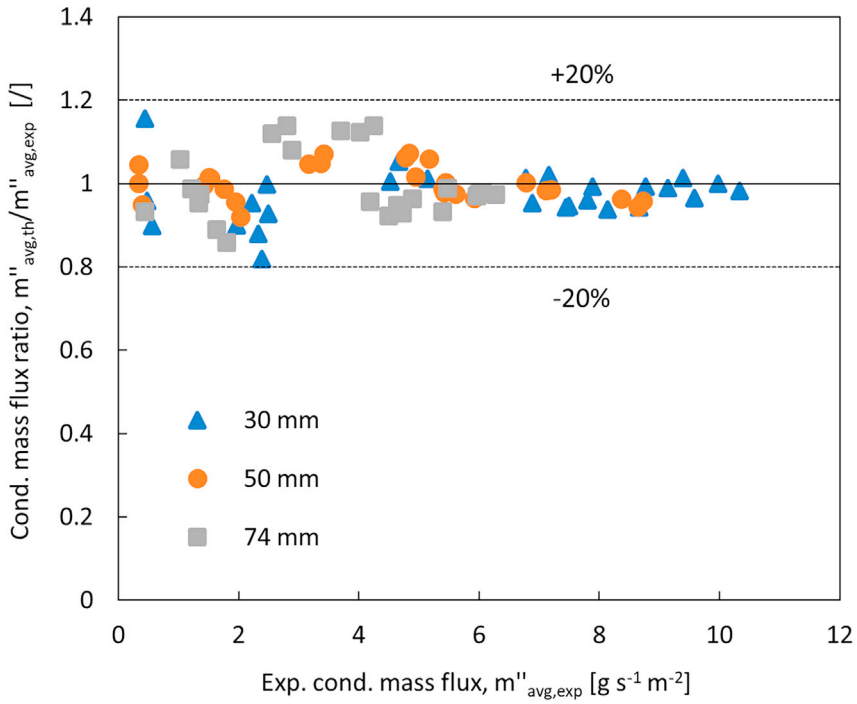

Figure 3. Experimental validation of the presented semi-empirical correlation

Comparison of theoretical and experimental condensate mass flux ratios for vertical flat plates with three different heights L = 30, 50, and 74 mm with respect to experimental condensate mass flux.

The applicable range of the presented semi-empirical correlation with respect to L, $T_{a,b}$, T_w, $W_{1,b}$, $Re_{a,b}$, Re_δ, and $Sc_{a,i}$ is 0.03–0.074 m, 29.5–77.3°C, 10.5–58.9°C, 0.683–0.974, 1,362–5,180, 0.06–2.51, and 0.622–0.630, respectively. The calculation procedure of values $Re_{a,b}$ and Re_δ can be found in STAR methods.

During our theoretical study, all the thermodynamic properties of humid air and water were calculated using the CoolProp functions—HAPropsSI function for humid air and PropsSI function for water and dry air (Bell et al., 2014).

Experimental validation of new semi-empirical correlation

An experimental validation of the proposed new semi-empirical correlation was performed by comparison of the predicted and experimental condensate mass fluxes. The experimental setup used for condensate mass flux measurements is presented in detail in STAR methods and Figures S1–S3 and Table S1. To ensure validity of experimental results, we performed two additional tasks: (1) evaluation of the condensation rate without the test section within the experimental setup (see STAR Methods) and (2) evaluation of the condensation process on test section's side walls (see STAR Methods and also see Figures S7 and S8, Table S2 and Table 4 in Poredoš et al. [2021a]).

Figure 3 shows condensate mass flux ratios $m''_{avg,th}/m''_{avg,exp}$ in relation to experimental condensate mass fluxes. The validation encompasses all 78 experimental points with all three heights of the vertical plates L = 30, 50, and 74 mm.

Considering all values, the agreement between the predicted and measured values is excellent, as 90% of theoretical values lies between ±12% of the mentioned ratio. This indicates that the presented correlation successfully accounts different thermal-hydraulic parameters, different heights of the vertical flat plates, and different air mass fractions inside the humid air in the bulk flow. The root-mean-square error (RMSE) of the correlation with respect to experimental values in the case of L = 30, 50, and 74 mm was 7.2%,

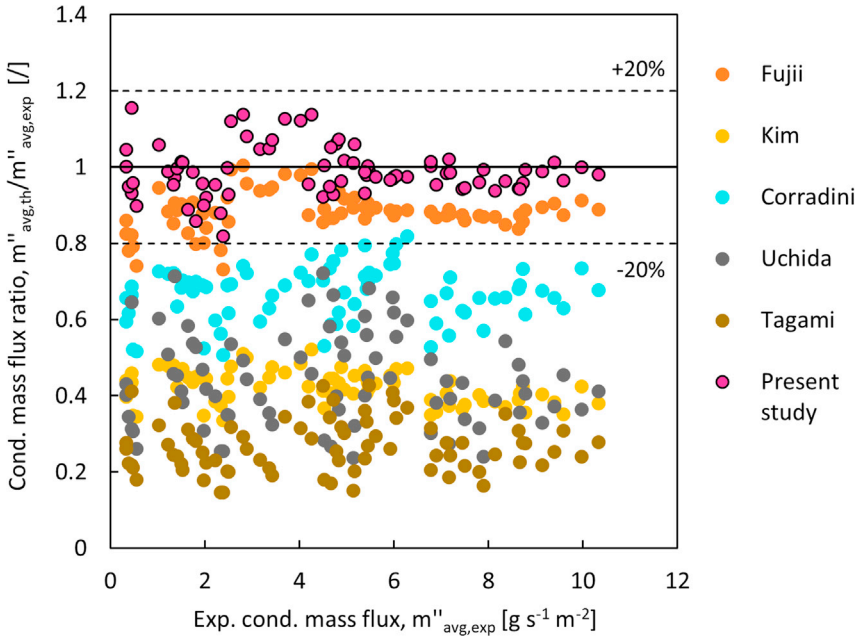

Figure 4. Comparison between the theoretical and experimental condensate mass fluxes predicted by existing correlations from the literature and new correlation

4.4%, and 8.1%, respectively. Overall, the results of an experimental validation of the correlation also justifies temperature measurements of a test section's side wall in the case of 50 mm height. The RMSE in the case of 30 and 74 mm heights is not far off from experimental values, confirming this decision.

Slightly larger discrepancies between theoretical and experimental values at low mass fluxes, i.e., below 5 g s^{-1} m^{-2} in comparison with the discrepancies above this value can be observed, regardless of the plate height. The main culprit for larger deviations could be lower temperature differences between humid air and the vertical plates. Lower temperature difference leads to lower condensate mass flux values, but the main contribution for larger deviations could be larger relative measurement uncertainties related to mentioned small temperature differences.

Tabulated experimental values denoting condensate mass flux at different operating conditions, i.e., temperature of humid air bulk flow ($T_{a,b}$), temperature difference between humid air bulk flow and the walls of hollow channels ($T_{a,b}$ - T_w), and volume flow of humid air ($\dot{V}_{a,b}$) for all three heights of vertical plates, 74, 50, and 30 mm, are available in Tables 1–3 in Poredoš et al. (2021a).

Comparison with existing correlations from the literature

A new correlation, presented in this study was evaluated against existing correlations from the literature that studied the condensate mass flux calculation on the vertical flat plate. The existing correlations are listed in our previous work related to the condensation of humid air on vertical flat plates and on horizontal tubes (Poredoš et al., 2021b) along with their applicable ranges of operating conditions. All the existing correlations were evaluated by also considering the condensation of humid air on side walls of the test section (see STAR Methods).

Three main observations based on the data in Figures 4 and 5 can be made. First, all the existing correlations underpredict the condensate mass flow fluxes, with the following range of RMSE encompassing all data: 12.7%–73.5% (Figures 4 and 5 and Table 1). Second, according to Figure 5 the predicted values based on existing correlations demonstrate worse agreement in the case of extremely high air mass fractions inside the bulk of humid air, i.e., $W_{1,b} > 0.9$. Third, all correlations demonstrate lower agreement with the lower height of the vertical flat plates. Range of RMSEs for the height of 74 mm 8.8%–66.0% with the average value of 38% confirms this observation, as the range of RMSEs for the height of vertical flat plates of 30 mm is larger 11.6%–78.8% with the average value of 49%.

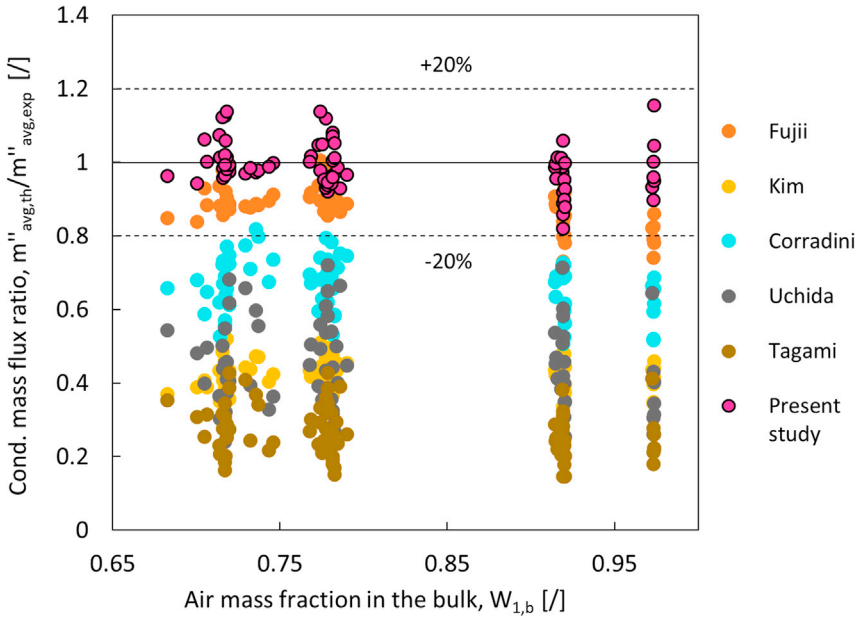

Figure 5. Condensate mass flux ratio with respect to air mass fraction in the bulk humid air, calculated by existing correlations from the literature and presented correlation

According to Figure 4, the evaluation of existing correlations from the literature shows that the problem of the humid air condensation on a series of vertical flat plates can be reasonably predicted by Fujii's numerical model (Fujii, 1991) (RMSE encompassing all data: 12.7%, Table 1). The second important consideration related to Fujii's numerical model is also a more complex definition of the temperature at the liquid-gas interface, which inherently increases computational time in comparison with our presented approach to calculate this value. Also, the presented correlation shows better agreement with the experimental data with the RMSE covering all data: 6.5%, Table 1, especially in the case of significantly higher air mass fractions inside the bulk of humid air, as demonstrated in Figure 5. These results confirm that the presented correlation, coupled with the experimentally extended factor that accounts the non-condensing component (air) in humid air (see Figures S5 and S6), significantly improves the prediction accuracy compared with the baseline non-extended correlation.

Correlations based on the stagnant diffusion film layer model, proposed by Corradini (1984) and Kim (Kim and Corradini, 1990), deviate significantly more with the overall RMSE of 34.1% and 57.8%. The Corradini correlation is sometimes in good agreement with experimental data, as some predicted values are within $\pm$20% of the mass flux ratio, $m''_{avg,th}/m''_{avg,exp}$. Finally, very simple semi-empirical correlations, proposed by Uchida (Uchida et al., 1965) and Tagami (1965), show a dissatisfactory agreement between experimental and theoretical values, with the overall RMSEs of 57.1% and 73.5%, respectively. As both correlations only consider the air to steam mass ratio ($h_{Uchida} = 379(m_{air}/m_{steam})^{-0.707}$ and $h_{Tagami} = 11.4 + 284(m_{steam}/m_{air})$), larger discrepancies are expected. Also, both simple correlations consider only free convection; therefore, in the case of water vapor condensation in circumstances with forced convection both mentioned correlations should be omitted from any analysis. Peterson (1996) argued that, even though the correlation by Uchida has been extensively used in the nuclear industry for the condensate mass flux rates calculations, the good performance of this correlation was found to be an artifact.

DISCUSSION

In this study, the condensation of water vapor in the presence of air as an NCG was theoretically and experimentally studied. The theoretical part of the study involved the development of a new semi-empirical correlation that describes condensation of humid air on a series of vertical flat plates forming vertical channels in circumstances with forced convection. The presented correlation separately considers the condensate flow, bulk flow of humid air as a laminar flow of a fluid over an isothermal plate, and the air as a non-condensing component of humid air. The experimental part of the study was performed on a custom-made experimental setup, based on a closed air loop. The main highlight of the setup were custom-made test sections with water-cooled 30-, 50-, and 74-mm

Table 1. RMSE [%] of the present and existing correlations from the literature

	Correlation					
Experiment	Fujii (Fujii, 1991)	Kim et al. (Kim and Corradini, 1990)	Corradini (Corradini, 1984)	Uchida et al. (Uchida et al., 1965)	Tagami (Tagami, 1965)	Present study
30 mm	14.3	61.8	39.8	67.1	78.8	7.2
50 mm	11.9	57.2	33.6	57.2	74.3	4.4
74 mm	11.7	53.8	26.8	42.8	66.0	8.1
All data	12.7	57.8	34.1	57.1	73.5	6.5

vertical flat plates that could allow the re-use of the condensing heat. Main contributions of this study are summarized with the following key points:

1. Existing correlations that account air as a non-condensing gas are not accurate in the case of higher values of air mass fractions inside the bulk flow of humid air. Here we successfully demonstrated an extension of applicable range of the existing correlations from the literature, with the extension of air mass fractions from 0.906 to 0.974. Such conditions exist often in the air conditioning domain; hence the proposed study could contribute an important insight into the humid air condensation process in real-world air-conditioning applications.
2. The literature lacks simple, practical, easy to implement, and computationally efficient correlations that consider condensation of humid air in the presence of air on a series of vertical flat plates forming vertical channels in circumstances with forced convection.
3. Within the paper we discuss the importance of the humid air flow classification inside the vertical channels. The test sections used in the experimental part of the study were designed by considering the velocity, thermal and concentration boundary layers thicknesses versus inter-channel dimensions. Therefore, we successfully demonstrated that the condensate mass flux of humid air on vertical flat plates forming vertical channels can be theoretically determined with a satisfactory agreement by considering external flow of humid air over the cooled vertical flat plates forming a vertical channel, only if the boundary layers do not merge between two neighboring plates. Namely, at a certain distance between two plates, the flow and related boundary layers along a particular plate correspond to external flow, as the bulk flow of humid air between two plates exists.
4. The presented new semi-empirical correlation, based on external humid air flow assumption, accurately predicts condensate mass fluxes in the case of different heights of vertical plates and thermal-hydraulic parameters, as 90% of predicted values are within $\pm 12\%$ ($m''_{avg,th}/m''_{avg,exp}$) of the experimental data.
5. The evaluation of existing correlations that consider condensation of water vapor in the presence of air on vertical flat plates revealed a wide range of accuracies, from 12.7% to 73.5% in terms of root-mean-square error (RMSE) encompassing all experimental data of this study.

The applicable range of this theoretical and experimental study with respect to plate height, temperatures of humid air and plate's wall, air mass fraction in humid air, Reynolds and Schmidt numbers of humid air is 0.03–0.074 m, 29.5–77.3°C, 10.5–58.9°C, 0.683–0.974, 1,362–5,180, and 0.622–0.630, respectively.

The main advantages of the presented correlation are its simplicity, ease of implementation in computer code, and short computational times. The correlation can be therefore easily used for a wide range of real-world applications, where the condensation of humid air plays important role in practical and also more complex situations.

Potential applications of the new correlation

The proposed semi-empirical correlation is generalized, thereby it can be used within various scientific and industrial applications where water vapor condensation occurs. Within this article we focus on the demonstration of the potential condenser performance that could be used for fresh water generation during the

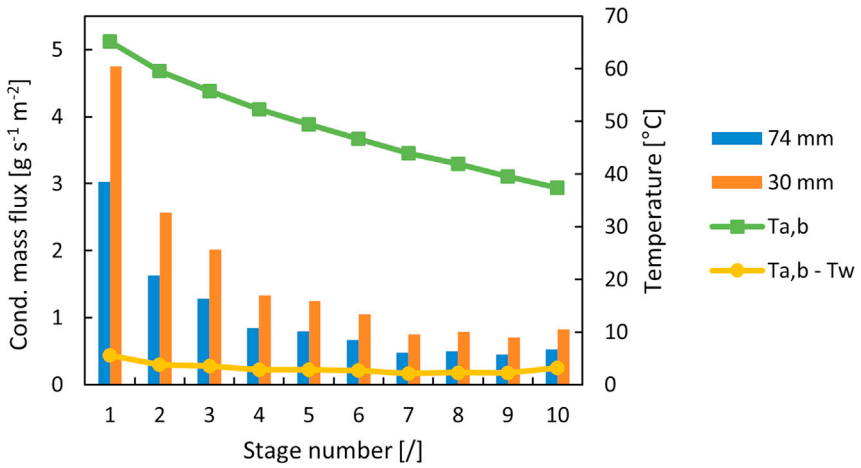

Figure 6. Performance of the potential condenser for the application of the seawater desalination

Performance of the potential condenser during the seawater desalination with similar operating conditions, as found during the outdoor experiment with the ten-stage thermally localized multistage solar still prototype (Xu et al., 2020).

seawater desalination and adsorption-based AWH. For this purpose, we relied on the data from two recent experimental studies in mentioned scientific research areas (LaPotin et al., 2021; Xu et al., 2020). Even though the focus of listed research studies was on the development of small-scale laboratory devices, the newly proposed concepts of fresh water generation, either from seawater or atmosphere, might be deployed in future medium- to large-scale applications. In that case the condensation of water vapor could be intensified by leveraging the force convection condensation.

To evaluate the potential condenser performance in circumstances with the force convection, the temperature of the humid air bulk flow ($T_{a,b}$) and the temperature of the cold wall (T_w) were determined from both studies. According to Figure 2, the calculation of the condensate mass fluxes requires two additional variables: the heights of vertical flat plates (L) and the velocity of the humid air bulk flow ($U_{a,b}$). We have chosen two heights, 30 and 74 mm, and the velocity at 1 m/s. In all cases the saturated air is assumed.

Here we note that the operating conditions during the fresh water generation during seawater desalination and adsorption-based AWH may largely deviate from the real-world applications. The temperature gradient among the stages could differ significantly owing to different geometry of the whole system, vapor generation system, and considered condensation in circumstances with forced convection. Therefore, the main purpose of this article is to show the possible application and the usability of the developed semi-empirical correlation that can accurately predict the performance of the proposed condenser.

Condenser performance evaluation for seawater desalination application

The temperatures of the humid air bulk flow and the cold wall were determined from Figure 6C in (Xu et al., 2020), which shows the outdoor experimental setup and the corresponding results of the ten-stage thermally localized multistage solar still prototype. We have chosen a single time point at approximately 1.8 h. The temperature gradient among all ten stages were determined and are listed in Table 2.

Based on the listed temperatures, Figure 6 shows the performance of the potential condenser with two different heights of vertical flat plates during the desalination process in circumstances with forced convection. As is evident from Figure 6, the main driving force behind the condensate mass flux rates are the temperatures of the humid air bulk flow ($T_{a,b}$). The temperatures show a near-linear trend; however, the mass flux rates show a clear power functional relation across the stages.

The condensate mass flux rates in stages seven to ten are almost identical with small difference. A slight increase of condensation rate between the mentioned stages can be observed, as stage ten shows higher mass flux rate (0.83 g s^{-1} m^{-2}) in comparison with stages seven, eight, and nine at 0.75, 0.78, and 0.70 g s^{-1}

Table 2. Temperatures of the humid air bulk flow ($T_{a,b}$) and the cold wall (T_w) during the outdoor experiments with the ten-stage thermally localized multistage solar still prototype

Stage number	$T_{a,b}$ [°C]	T_w [°C]
1	65.2	59.6
2	59.6	55.8
3	55.8	52.3
4	52.3	49.5
5	49.5	46.7
6	46.7	44.0
7	44.0	41.9
8	41.9	39.6
9	39.6	37.4
10	37.4	34.2

Xu et al. (2020).

m^{-2}, respectively, for the case of the vertical flat plates height of 74 mm. The main reason is relatively low temperature of the humid air bulk flow, as in this case the condensate mass flux rates are highly sensitive to the temperature difference between humid air and the cold surface ($T_{a,b}$ - T_w). Even though the temperature of the humid air in stage seven is considerably larger at 44.0°C in comparison with stage ten with the humid air temperature 37.4°C, the higher temperature difference for the case of stage ten prevails (tenth stage: 3.2°C versus seventh stage: 2.1°C).

If the height of the vertical flat plates is reduced from 74 to 30 mm, the overall condensate mass flux referring to all ten stages increases by 57% (10.2 g s^{-1} m^{-2} for 74 mm versus 16.0 g s^{-1} m^{-2} for 30 mm).

Condenser performance evaluation for adsorption-based AWH application

Figure S9 in LaPotin et al. (2021) shows the temperature distribution across the dual-stage adsorption-based AWH device during the outdoor experiments. The evaluation of the potential condenser performance was performed for four different points at the following times: 10:00, 12:00, 14:00, and 16:00. Table 3 shows the corresponding temperatures of the humid air bulk flow ($T_{a,b}$) and the temperature of the cold wall (T_w).

Similar to findings described for the seawater desalination application, the largest impact on the condensate mass flux rates is related to the temperature of the humid air bulk flow, as demonstrated in the Figure 7. Relative differences for the first stage between 12:00, 14:00, and 16:00 are enormous in terms of mass flux rates at 131%, 253%, and 100%, respectively, while the temperatures of the humid air at mentioned time points are 84.1°C, 91.3°C, and 80.2°C. The relative differences are averaged based on the results for 30 and 74 mm heights of the vertical flat plates of the potential condenser. The main reason is the water vapor capacity

Table 3. Temperatures of the humid air bulk flow ($T_{a,b}$) and the cold wall (T_w) during the outdoor experiments with the dual-stage adsorption-based atmospheric water harvesting device

Time	Stage number	$T_{a,b}$ [°C]	T_w [°C]
10:00	1	36.8	30.2
10:00	2	29.4	27.4
12:00	1	84.1	60.9
12:00	2	58.6	32.6
14:00	1	91.3	65.1
14:00	2	62.8	32.1
16:00	1	80.2	57.2
16:00	2	55.7	30.2

LaPotin et al. (2021)

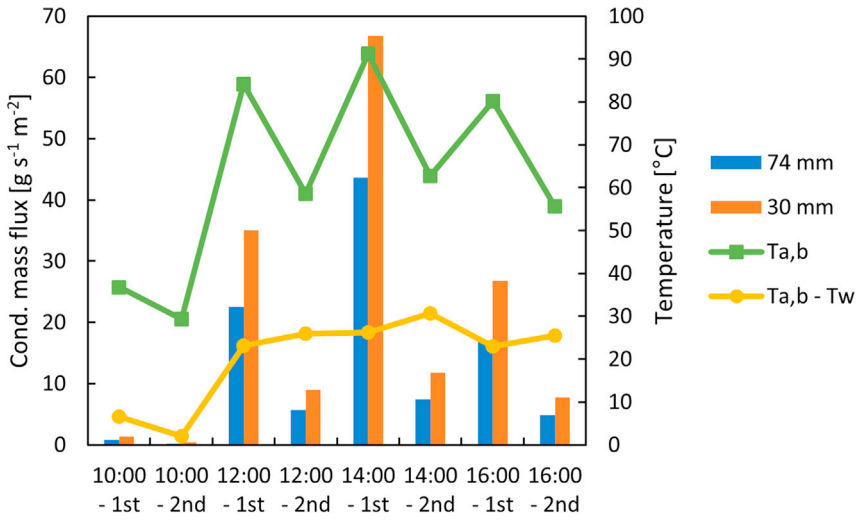

Figure 7. Performance of the potential condenser for the application of the adsorption-based atmospheric water harvesting

Performance of the potential condenser during the adsorption-based atmospheric water harvesting with similar operating conditions, as found during the outdoor experiment with the dual-stage adsorption-based atmospheric water harvesting device (LaPotin et al., 2021).

of air at certain humid air temperatures, increasing significantly with higher air temperatures. Thereby at moderately lower humid air temperatures at 58.6°C, 62.8°C, and 55.7°C, corresponding to the same time points as before, the second stage demonstrates considerably lower relative differences of condensate mass flux rates at 116%, 152%, and 100% (again averaged values based on the results for 30 and 74 mm).

Limitations of the study

The first limitation of the study is the relatively low maximum temperature of the humid air bulk flow at 77.3°C, which is inherently related to the used experimental setup. In the future upgrade of the presented experimental setup could be performed, with the temperatures of the humid air bulk flow reaching 95°C. As demonstrated within the article related to the potential applications of the new correlation, in real-world applications the temperatures of the humid air can clearly exceed 90°C. Knowing that the condensate mass flux is significantly higher at humid air temperatures reaching 95°C, future studies should focus more on this aspect.

Besides, the test section's side walls are made of copper and in direct contact with the cold vertical flat plates, thereby increasing the condensate mass flux rates on side walls. However, to increase the condenser's ability in terms of latent heat re-use, the majority of the humid air condensation should occur on vertical flat plates that form a hollow channel with the cooling water flowing inside. The key to improve the amount of recycled latent heat lies in material science, as two solutions are possible: (1) to consider the low thermally conductive material for the side walls, where the contact between this material and the hollow copper channels is possible; (2) superhydrophobic coating for anti-condensation properties for side walls. The latter property is of high importance for the future systems dealing with high-temperature humid air, as adequate thermal insulation backed up by anti-condensation coating could provide the highest possible re-use of the latent heat, released during the condensation process in real-world applications.

STAR★METHODS

Detailed methods are provided in the online version of this paper and include the following:

- KEY RESOURCES TABLE
- RESOURCE AVAILABILITY
  - Lead contact
  - Materials availability
  - Data and code availability

SUPPLEMENTAL INFORMATION

Supplemental information can be found online at https://doi.org/10.1016/j.isci.2021.103565.

ACKNOWLEDGMENTS

This work was supported by the Fellowship of China Postdoctoral Science Foundation (No. 2020TQ0186); the Belt and Road Young Scientists Exchange Program of Shanghai Science and Technology Committee (No. 20160742700); the Industrial project, Research and development in heat and mass processes in household appliances, Gorenje, 2017–2020; the state budget by the Slovenian Research Agency (Program/Project Nr. P2-0223).

AUTHOR CONTRIBUTIONS

Conceptualization: P.P., N.P., B.V., and A.K.; methodology: P.P. and T.Ž.; software: P.P., T.Ž., and Q.M.; validation: P.P. and A.K.; formal analysis: P.P., N.P., and B.V.; investigation: B.V.; resources: N.P.; data curation: P.P. and T.Ž.; writing – original draft: P.P.; visualization: P.P.; supervision: R.W. and A.K.; project administration: P.P. and A.K.; funding acquisition: R.W. and A.K.

DECLARATION OF INTERESTS

The authors declare that they have no known competing financial interests or personal relationships that could have appeared to influence the work reported in this paper.

Received: September 6, 2021
Revised: November 18, 2021
Accepted: December 1, 2021
Published: January 21, 2022

REFERENCES

Ait Hssain, M., Armou, S., Zine-Dine, K., Mir, R., and El Hammami, Y. (2021). Numerical investigation of influence of nanoparticles presence on water vapor condensation process inside a vertical channel. J. Nanomater. *2021*. https://doi.org/10.1155/2021/5547172.

Ait Hssain, M., El Hammami, Y., Mir, R., Armou, S., and Zine-Dine, K. (2019). Numerical analysis of laminar convective condensation with the presence of noncondensable gas flowing downward in a vertical channel. Math. Probl. Eng. *2019*. https://doi.org/10.1155/2019/7941363.

Asano, K. (2006). Mass Transfer: From Fundamentals to Modern Industrial Applications (John Wiley & Sons). https://doi.org/10.1002/3527609180.

Asano, K., Nakano, Y., and Inaba, M. (1979). Forced convection film condensation of vapors in the presence of noncondensable gas on a small vertical flat plate. J. Chem. Eng. Jpn. *12*, 196–202. https://doi.org/10.1252/jcej.12.196.

Bell, I.H., Wronski, J., Quoilin, S., and Lemort, V. (2014). Pure and pseudo-pure fluid thermophysical property evaluation and the open-source thermophysical property library coolprop. Ind. Eng. Chem. Res. *53*. https://doi.org/10.1021/ie4033999.

Bergman, T.L., Incropera, F.P., DeWitt, D.P., and Lavine, A.S. (2011). Fundamentals of Heat and Mass Transfer (Wiley).

Bum-Jin, C., Sin, K., Min Chan, K., and Ahmadinejad, M. (2004). Experimental comparison of film-wise and drop-wise condensations of steam on vertical flat plates with the presence of air. Int. Commun. Heat Mass Transf. *31*, 1067–1074. https://doi.org/10.1016/j.icheatmasstransfer.2004.08.004.

Cao, R., Ruan, R., Tan, H., Bai, S., Du, Y., and Liu, H. (2021). Condensational growth activated by cooling method for multi-objective treatment of desulfurized flue gas: a full-scale study. Chem. Eng. J. *410*. https://doi.org/10.1016/j.cej.2020.128296.

Cengel, Y.A., and Ghajar, A.J. (2015). Heat and Mass Transfer: Fundamentals and Applications, Fifth Edition (McGraw-Hill Education).

Charef, A., Feddaoui, M., Alla, A.N., and Najim, M. (2017). Numerical study of humid air condensation in presence of non-condensable gas along an inclined channel. In Energy Procedia (Elsevier Ltd), pp. 128–133. https://doi.org/10.1016/j.egypro.2017.11.185.

Chen, X., Liu, J., Ma, Y., Wang, P., Bai, X., and Pan, J. (2020). Large-scale and low-cost fabrication of two functional silica sorbents by vapor condensation induced nanoemulsions and their excellent uptake performance. Chem. Eng. J. *379*. https://doi.org/10.1016/j.cej.2019.122364.

Chougule, S.S., and Sahu, S.K. (2016). Comparative study on heat transfer enhancement of low volume concentration of Al2o3-water and carbon nano-tube-water nano-fluids in transition regime using helical screw tape inserts. Exp. Heat Transf. *29*. https://doi.org/10.1080/08916152.2014.926432.

Corradini, M.L. (1984). Turbulent condensation on a cold wall in the presence of a noncondensable gas. Nucl. Technol. *64*, 186–195. https://doi.org/10.13182/NT84-A33341.

Denny, V.E., and Mills, A.F. (1969). Nonsimilar solutions for laminar film condensation on a vertical surface. Int. J. Heat Mass Transf. *12*. https://doi.org/10.1016/0017-9310(69)90158-6.

Ejeian, M., and Wang, R.Z. (2021). Adsorption-based atmospheric water harvesting. Joule. https://doi.org/10.1016/j.joule.2021.04.005.

Faghri, A., and Zhang, Y. (2020). Fundamentals of Multiphase Heat Transfer and Flow (Springer). https://doi.org/10.1007/978-3-030-22137-9.

Farooq, A.S., Zhang, P., Gao, Y., and Gulfam, R. (2021). Emerging radiative materials and prospective applications of radiative sky cooling - a review. Renew. Sustain. Energy Rev. https://doi.org/10.1016/j.rser.2021.110910.

Fujii, T. (1991). Theory of Laminar Film Condensation, First Edition (Springer-Verlag New York). https://doi.org/10.1007/978-1-4612-3152-3.

Fuller, E.N., Schettler, P.D., and Giddings, J.C. (1966). A new method for prediction of binary gas-phase diffusion coefficients. Ind. Eng. Chem. *58*. https://doi.org/10.1021/ie50677a007.

Ganguli, A., Patel, A.G., Maheshwari, N.K., and Pandit, A.B. (2008). Theoretical modeling of condensation of steam outside different vertical geometries (tube, flat plates) in the presence of noncondensable gases like air and helium. Nucl. Eng. Des. *238*. https://doi.org/10.1016/j.nucengdes.2008.02.016.

Ge, M., Wang, S., Zhao, J., Zhao, Y., and Liu, L. (2016). Condensation of steam with high CO2 concentration on a vertical plate. Exp. Therm. Fluid Sci. *75*. https://doi.org/10.1016/j.expthermflusci.2016.02.008.

Gross, J.F., Hartnett, J.P., Masson, D.J., and Gazley, C. (1961). A review of binary laminar boundary layer characteristics. Int. J. Heat Mass Transf. *3*. https://doi.org/10.1016/0017-9310(61)90030-8.

Haechler, I., Park, H., Schnoering, G., Gulich, T., Rohner, M., Tripathy, A., Milionis, A., Schutzius, T.M., and Poulikakos, D. (2021). Exploiting radiative cooling for uninterrupted 24-hour water harvesting from the atmosphere. Sci. Adv. *7*, eabf3978.

Kakac, S., Shah, R., and Aung, W. (1987). Handbook of Single-Phase Convective Heat Transfer, 1st (Wiley-Interscience).

Karkoszka, K. (2007). Mechanistic Modelling of Water Vapour Condensation in Presence of Noncondensable Gases (KTH, School of Engineering Sciences).

Katopodes, N.D. (2018). Free-Surface Flow: Computational Methods (Butterworth-Heinemann). https://doi.org/10.1016/C2017-0-00542-6.

Kim, M.H., and Corradini, M.L. (1990). Modeling of condensation heat transfer in a reactor containment. Nucl. Eng. Des. *118*, 193–212. https://doi.org/10.1016/0029-5493(90)90057-5.

LaPotin, A., Zhong, Y., Zhang, L., Zhao, L., Leroy, A., Kim, H., Rao, S.R., and Wang, E.N. (2021). Dual-stage atmospheric water harvesting device for scalable solar-driven water production. Joule *5*. https://doi.org/10.1016/j.joule.2020.09.008.

Li, C., and Li, J. (2011). Laminar forced convection heat and mass transfer of humid air across a vertical plate with condensation. Chin. J. Chem. Eng. *19*, 944–954. https://doi.org/10.1016/S1004-9541(11)60076-1.

Liao, Y., and Vierow, K. (2006). A generalized diffusion layer model for condensation of vapor with noncondensable gases. J. Heat Transfer *129*, 988–994. https://doi.org/10.1115/1.2728907.

Ma, Q., Xu, Z., and Wang, R. (2021). Distributed solar desalination by membrane distillation: current status and future perspectives. Water Res. https://doi.org/10.1016/j.watres.2021.117154.

Martinez-Urrutia, A., Fernandez de Arroiabe, P., Ramirez, M., Martinez-Agirre, M., and Mounir Bou-Ali, M. (2018). Contact angle measurement for LiBr aqueous solutions on different surface materials used in absorption systems. Int. J. Refrig. *95*. https://doi.org/10.1016/j.ijrefrig.2018.05.041.

Naylor, D., and Friedman, J. (2010). Model of film condensation on a vertical plate with noncondensing gas. J. Thermophys. Heat Transf. *24*. https://doi.org/10.2514/1.43136.

Nusselt, W. (1916). Die Oberflächenkondensation des Wasserdampfes. Z. Vereins Deutsch. Ing. *60*, 541–546.

Othmer, D.F. (1929). The condensation of steam. Ind. Eng. Chem. *21*. https://doi.org/10.1021/ie50234a018.

Peterson, P.F. (1996). Theoretical basis for the Uchida correlation for condensation in reactor containments. Nucl. Eng. Des. *162*. https://doi.org/10.1016/0029-5493(95)01125-0.

Peterson, P.F., Schrock, V.E., and Kageyama, T. (1992). Diffusion Layer Theory for Turbulent Vapor Condensation with Noncondensable Gases (American Society of Mechanical Engineers, Heat Transfer Division, (Publication) HTD).

Poredoš, P., Petelin, N., Vidrih, B., Žel, T., Ma, Q., Wang, R., and Kitanovski, A. (2021a). Experimental condensate mass flux values during the condensation of water vapor from humid air inside vertical channels formed by flat plates. Mendeley Data *V1*. https://doi.org/10.17632/8zb3trjjgk.1.

Poredoš, P., Petelin, N., Žel, T., Vidrih, B., Gatarić, P., and Kitanovski, A. (2021b). Performance of the condensation process for water vapour in the presence of a non-condensable gas on vertical plates and horizontal tubes. Energies *14*. https://doi.org/10.3390/en14082291.

Roetzel, W., Luo, X., and Chen, D. (2019). Design and Operation of Heat Exchangers and their Networks (Academic Press). https://doi.org/10.1016/C2017-0-03210-X.

Saraireh, M., Li, J.D., and Thorpe, G. (2010). Modelling of heat and mass transfer involving vapour condensation in the presence of non-condensable gases. In 17th Australasian Fluid Mechanics Conference 2010 (University of Auckland), pp. 96–100.

Schlichting, H., and Gersten, K. (2016). Boundary-layer theory (Springer-Verlag Berlin Heidelberg). https://doi.org/10.1007/978-3-662-52919-5.

Siow, E.C., Ormiston, S.J., and Soliman, H.M. (2007). Two-phase modelling of laminar film condensation from vapour-gas mixtures in declining parallel-plate channels. Int. J. Therm. Sci. *46*. https://doi.org/10.1016/j.ijthermalsci.2006.07.001.

Siow, E.C., Ormiston, S.J., and Soliman, H.M. (2004). A two-phase model for laminar film condensation from steam-air mixtures in vertical parallel-plate channels. Heat Mass Transf. *40*, 365–375. https://doi.org/10.1007/s00231-003-0425-0.

Siow, E.C., Ormiston, S.J., and Soliman, H.M. (2002). Fully coupled solution of a two-phase model for laminar film condensation of vapor-gas mixtures in horizontal channels. Int. J. Heat Mass Transf. *45*. https://doi.org/10.1016/S0017-9310(02)00094-7.

SIST EN ISO 5167-2:2004 - Measurement of Fluid Flow by Means of Pressure Differential Devices Inserted in Circular Cross-Section Conduits Running Full - Part 2: Orifice Plates (ISO 5167-2:2003). https://standards.iteh.ai/catalog/standards/sist/6d437324-a8b6-4412-b17e-3f9111a114d1/sist-en-iso-5167-2-2004. 2003.

EN ISO 5801:2017 - Fans - Performance testing using standardized airways (ISO 5801:2017). https://www.iso.org/standard/56517.html. 2018.

Song, J.W., and Fan, L.W. (2021). Temperature dependence of the contact angle of water: a review of research progress, theoretical understanding, and implications for boiling heat transfer. Adv. Colloid Interf. Sci. https://doi.org/10.1016/j.cis.2020.102339.

Stephan, K., and Laesecke, A. (1980). The influence of suction on heat and mass transfer in condensation of mixed vapors. Wärme Stoffübertragung *13*. https://doi.org/10.1007/BF00997641.

Tagami, T. (1965). Interim Report on Safety Assessments and Facilities Establishment Project in Japan for Period Ending June 1965 (No. 1). https://www.osti.gov/servlets/purl/4436864.

Trosseille, J., Mongruel, A., Royon, L., and Beysens, D. (2021). Radiative cooling for dew condensation. Int. J. Heat Mass Transf. *172*. https://doi.org/10.1016/j.ijheatmasstransfer.2021.121160.

Uchida, H., Oyama, A., and Togo, Y. (1965). Evaluation of post-incident cooling systems of light water power reactors. In Proceedings of the Third International Conference on the Peaceful Uses of Atomic Energy (United Nations), pp. 93–102.

Wang, S., Yu, X., Liang, C., and Zhang, Y. (2018). Enhanced condensation heat transfer in air-conditioner heat exchanger using superhydrophobic foils. Appl. Therm. Eng. *137*. https://doi.org/10.1016/j.applthermaleng.2018.04.020.

Wang, W., Xie, S., Pan, Q., Dai, Y., Wang, R., and Ge, T. (2021). Air-cooled adsorption-based device for harvesting water from island air. Renew. Sustain. Energy Rev. *141*. https://doi.org/10.1016/j.rser.2021.110802.

Wu, X., Yang, F., Lu, G., Zhao, X., Chen, Z., and Qian, S. (2021). A breathable and environmentally friendly superhydrophobic coating for anti-condensation applications. Chem. Eng. J. *412*. https://doi.org/10.1016/j.cej.2021.128725.

Xu, J., Yu, Y., Yin, Y., Zhang, J., and Zhong, H. (2017). Heterogeneous condensation coupled with partial gas circulation for fine particles abatement. Chem. Eng. J. *330*. https://doi.org/10.1016/j.cej.2017.08.047.

Xu, K., Ren, S., Song, J., Liu, J., Liu, Z., Sun, J., and Ling, S. (2021). Colorful superhydrophobic concrete coating. Chem. Eng. J. *403*. https://doi.org/10.1016/j.cej.2020.126348.

Xu, Z., Zhang, L., Zhao, L., Li, B., Bhatia, B., Wang, C., Wilke, K.L., Song, Y., Labban, O., Lienhard, J.H., et al. (2020). Ultrahigh-efficiency desalination: via a thermally-localized multistage solar still. Energy Environ. Sci. *13*. https://doi.org/10.1039/c9ee04122b.

Yi, Q., Tian, M., and Fang, D. (2015). CFD simulation of air-steam condensation on an isothermal vertical plate. Int. J. Heat Technol. *33*, 25–32. https://doi.org/10.18280/ijht.330104.

Zanganeh, P., Goharrizi, A.S., Ayatollahi, S., Feilizadeh, M., and Dashti, H. (2020). Efficiency improvement of solar stills through wettability alteration of the condensation surface: an experimental study. Appl. Energy *268*. https://doi.org/10.1016/j.apenergy.2020.114923.

Zhang, L., Xu, Z., Zhao, L., Bhatia, B., Zhong, Y., Gong, S., and Wang, E.N. (2021). Passive, high-efficiency thermally-localized solar desalination. Energy Environ. Sci. https://doi.org/10.1039/d0ee03991h.

STAR★METHODS

KEY RESOURCES TABLE

RESOURCE	SOURCE	IDENTIFIER
Deposited data		
Note: The complete experimental dataset can be found in (Poredoš et al., 2021a)	(Poredoš et al., 2021a)	Mendeley Data: https://doi.org/10.17632/8zb3trjjgk.1
Software and algorithms		
CoolProp version 6.4.1	CoolProp	http://www.coolprop.org/index.html
Python 3.8.	Python Software Foundation	https://www.python.org/
Other		
Type K thermocouple	XF-1256-FAR	https://si.farnell.com/labfacility/z2-k-2-x-5/sensor-t-couple-k-z2-pk5/dp/8598150?st=type%20k%20thermocouple
Differential pressure transmitter	DDPT 20	https://www.materm.si/Prodajni_program/Diferencni_tlacni_pretvorniki
Digital humidity sensor SHT85 (RH/T)	SHT85	https://www.sensirion.com/en/environmental-sensors/humidity-sensors/sht85-pin-type-humidity-sensor-enabling-easy-replaceability/
Desktop scale	FKB 30K1A	https://www.kern-sohn.com/
National instruments	NI-9214	https://www.ni.com/sl-si/support/model.ni-9214.html
National instruments	NI-9219	https://www.ni.com/sl-si/support/model.ni-9219.html

RESOURCE AVAILABILITY

Lead contact

Further information and requests for resources should be directed to and will be fulfilled by the lead contact, Prof. Dr. Andrej Kitanovski (andrej.kitanovski@fs.uni-lj.si).

Materials availability

This study did not generate new unique materials.

Data and code availability

- Experimental data have been deposited at Mendeley Data and are publicly available as of the date of publication. DOI is listed in the key resources table. Additional data reported in this paper will be shared by the Lead Contact upon request.
- This paper does not report original code.
- Any additional information required to reanalyze the data reported in this paper is available from the Lead Contact upon request.

METHOD DETAILS

Nomenclature and units	
A	surface area [m^2]
c_p	specific heat of condensate [J kg^{-1} K^{-1}]
C	distance between the isothermal side walls and the first and last flat plate [m]
C	concentration [mol m^{-3}]
D	mass diffusivity [m^2 s^{-1}]

(*Continued on next page*)

Continued	
D	distance between two neighboring plates [m]
F	correlation accounting for non-condensing gas [/]
G	gravitational acceleration = 9.81 m s^{-2}
H	specific enthalpy [J kg^{-1}]; condensation heat transfer coefficient [W m^{-2} K^{-1}]
J	diffusive vapor flux [kg s^{-1} m^{-2}]
K	thermal conductivity [W m^{-1} K^{-1}]
L	plate height [m]
M	exponential function [/]; mass [kg]
$\dot{m}$	mass flow [kg s^{-1}]
m''	mass flux [kg s^{-1} m^{-2}]
M	molecular mass [kg mol^{-1}]
N	vapor mass flux [kg s^{-1} m^{-2}]
P	pressure [kPa]
q''	condensate heat flux [J m^{-2}]
R	Ratio of condensate and vapor properties [/];
T	temperature [°C, K]
U	velocity [m s^{-1}]
V	atomic diffusion volume [m^3 mol^{-1}]
$\dot{V}$	volume flow [m^3 s^{-1}]
W	mass fraction [/]
x	coordinate of two-dimensional Cartesian coordinate system [/]
y	coordinate of two-dimensional Cartesian coordinate system [/]
Y	mass fraction-difference ratio

Greek letters	
β	constant [/]; mass transfer coefficient [m s^{-1}]
Γ	mass flow of condensate per unit width of the plate [kg s^{-1} m^{-1}]
δ	condensate thickness [m]; boundary layer thickness [m]
μ	dynamic viscosity [kg s^{-1} m^{-1}]
ν	kinematic viscosity [m^2 s^{-1}]
ρ	density [kg m^{-3}]
τ	shear stress [Pa]
φ	constant [/]

Subscripts, superscripts	
1	non-condensable gas (air)
2	condensing component (water vapor)
a	humid air; absolute
amb	ambient
avg	average
b	bulk
c	condensation; condensate
C	concentration
cont	contact
dew	dew-point
edge	edge

(*Continued on next page*)

Continued	
error	error
exp	experimental
fg	vaporization
i	liquid-gas interface
in	inlet
m	exponential function
main	main
mid	middle
new	new
out	outlet
p1-3	part one to three
R	ratio of air mass fractions
side-w	side wall
t	thermal
th	theoretical
tot	total
up	up
v	velocity
V	humid air inside the vapour boundary layer
w	plate wall

Dimensionless quantities	
Nu	Nusselt number
Pr	Prandtl number
Re	Reynolds number
Sc	Schmidt number
Sh	Sherwood number

Experimental setup

Experimental part of the study has been performed on a custom-made experimental setup, based on a closed air loop, as shown in Figures S1 and S2. It consists of the following parts: 1 - test section, 2 - humidifier chamber, 3, 6 - air heater, 4 – orifice meter, 5 – radial ventilator, 7 – condensate collector with high precision weighing scale and 8 – temperature-controlled water bath.

Humid air was flowing in the downward direction over the cooled vertical flat plates within the test section (1), as demonstrated in Figure S3B). Condensate was collected on the bottom of the setup and weighted by the high precision weighing scale (Desktop scale, FKB 30K1A) with the accuracy of $\pm$0.05 g (7). Dehumidified air was then heated for the first time by air heater (Veab, model CV, nominal heating power 2.7 kW) (6). The volume flow of the dehumidified air was determined using the orifice meter (4) according to SIST EN ISO 5801 (EN ISO 5801:2017) and SIST EN ISO 5167-2 (SIST EN ISO 5167-2:2004). The diameter ratio β and accuracy of the orifice meter were 0.596 and $\pm$0.8%, respectively. Approximately 0.13 m before the orifice meter, one combined temperature and humidity sensor (SHT85) was placed with the temperature and humidity accuracies of $\pm$0.3 K and $\pm$1.8%, respectively. The corresponding pressure drop before and after the orifice meter was measured using differential pressure transmitters (DDPT 20) with the measuring range 0–250 Pa and accuracy of $\pm$0.8%. The dehumidified air was heated for the second time by additional air heater (Veab, model CV, nominal heating power 2.7 kW) (3) and then humidified within the humidifier chamber (2) consisting of a high pressure and a fine nozzle orifice. The relative humidity of the humid air at the inlet at the test sections was 100%. As the system produced water droplets with an estimated diameter of 10 - 15 μm, the removal of larger water droplets was handled by drift eliminators before the inlet at the test sections. The cooling water was prepared in a temperature-controlled water bath and circulated in a closed loop. All the measurements have been performed at ambient pressure, i.e. p_{amb} = 101.325 kPa.

A measurement console (National Instruments, NI-9214 and NI-9219) was used to acquire the temperature measurements of humid air and condensing walls of vertical plates on 11 measuring points with the K-type bare-wire thermocouples (XF-1256-FAR) with outer diameters of 0.2 mm and measurement uncertainty of $\pm$0.2 K. To measure the humid air temperature, eight thermocouples were positioned at the test section inlet and outlet locations [Figure S3A)]. Condensing wall temperature measurements were acquired in the middle of vertical flat plate, as shown in [Figure S3A)].

During the experiments air was used as a non-condensable gas. The air mass fraction was determined based on the fixed value of relative humidity, which was always 100%. The controller of the humidifier chamber was measuring the relative humidity of the humid air and adjusted the amount of generated water droplets accordingly.

The test sections were made of four copper side walls with the inner dimensions of 312 × 212 mm^2 (Figure S3). Four copper hollow channels with the dimensions of 212 × 12 mm^2 were inserted through larger sides of the test section. Each hollow channel had two circular fittings with the inner and outer diameters of 33 and 35 mm, respectively, located at the cooling water inlet and outlet. The distance between two neighboring plates forming a vertical channel was 66 mm, while the distance between the isothermal side walls and the first and last flat plate was 33 mm, as illustrated in Figure S3A). The heights of vertical flat plates of each test section were 30, 50 and 74 mm [Figure S3A)]. All other geometrical characteristics of all three test sections are provided in Table S1.

Flow configuration of each test section was crossflow, as cooling water flowed inside each hollow channel in the horizontal direction, while humid air flowed in the downward direction. The total number of vertical plates in all cases were 8. The thickness of all walls of test sections including walls of hollow channels were 1 mm. All major exposed surfaces of an experimental setup were insulated to minimize the heat losses and the non-intentional condensation of water vapor on the inner surfaces of the experimental setup. The thickness of the insulation was 13 mm with the thermal conductivity $\leq$0.036 W m^{-1} K^{-1}.

Condensation rate without the test section. Even though the experimental setup has been extensively insulated, we observed condensation on the inner surfaces of the vertical part of the test setup during trial measurements. To account for the additional condensation between locations 2 and 7 on Figure S1, we made separate experiments with the test sections swapped by the conventional duct. A set of measurements was done within the temperature range of humid air between 30 and 75°C. The main purpose of those experiments was to evaluate the measuring error during the condensate mass flow measurements in the test chamber. Based on a set of measurements, the following correlation (units, g s^{-1}) has been determined:

$$\dot{m}_{exp,error} = -0.0017 \cdot \frac{(T_{a,in} + T_{a,out})}{2} - 0.0356 \qquad \text{(Equation 11)}$$

where $T_{a,in}$ and $T_{a,out}$ are humid air temperatures at the inlet and outlet of the test section, respectively. All experimental values denoting condensate mass flux reported here include the correction, provided by Equation 11.

Range of $Re_{a,b}$ and Re_{δ}. Humid air inside the test section flows in the downward direction, as shown in the Figure S3. By passing the vertical flat plates, the water vapor condenses on the cooled walls. To further confirm the approach of the presented correlation by considering the laminar flow of a fluid over an isothermal plate, we calculated the Reynolds number of the humid air flowing past the plate. The Reynolds number was calculated using the equation:

$$Re_{a,b} = \frac{\rho_{a,b} U_{a,b} L}{\mu_{a,b}} \qquad \text{(Equation 12)}$$

where $\rho_{a,b}$, $U_{a,b}$, $\mu_{a,b}$ represent density, inlet velocity and dynamic viscosity of humid air in the bulk flow, respectively. The calculation of the $Re_{a,b}$ number encompassing all the experimental points, at which measurements have been performed, shows that the range of $Re_{a,b}$ number is between 1362 and 5180, with an order of magnitude 1.5-5 × 10^3 indicating laminar regime, which is up to $Re_{a,b}$ = 5 × 10^5 (Bergman et al., 2011).

During the condensation process, the flow of the liquid film (condensate) may exhibit laminar (wave-free), laminar (wavy) or turbulent regime (Cengel and Ghajar, 2015). The regime depends on the Reynolds number of the condensate, which can be calculated as (Faghri and Zhang, 2020):

$$Re_{\delta} = \frac{4\Gamma}{\mu_c} \quad \text{(Equation 13)}$$

where μ_c is the dynamic viscosity of the condensate and Γ is the mass flow of condensate per unit width of the plate, calculated as:

$$\Gamma = m''_{avg,exp}\, L \quad \text{(Equation 14)}$$

The calculated range of experimental condensate Reynolds number Re_{δ}:0.06-2.51 confirm the laminar (wave-free) regime of the condensate, defined at Re_{δ} <30 (Bergman et al., 2011).

Boundary layer thicknesses evaluation

During the external flow of humid air over the cold flat plate, where the condensation of water vapor occurs, two distinctive regions are formed: free stream, denoting the bulk flow of humid air and three types of gaseous boundary layers: velocity, thermal and concentration. Inside the velocity boundary layer, velocity gradients and shear stresses are large, while in the case of thermal and concentration boundary layers, larger temperature and concentration gradients can be observed. With the increasing distance between two parallel plates forming a channel, the internal flow regime becomes less pronounced. Therefore, at a certain distance between two plates, the flow and related boundary layers along a particular plate correspond to external flow, as the bulk flow of humid air between two plates exists. Inside the humid air bulk flow the effects of velocity gradient, shear stress, temperature and concentration gradient are negligible.

In the literature, two distinctive types of velocity boundary layers can be found (Schlichting and Gersten, 2016): (i) boundary-layer thickness and (ii) displacement thickness. The first one has been introduced arbitrarily, while the second one is a more correct and fluid mechanically interpretable measure for the boundary layer thickness. Both are defined in a similar way using same variables (Equation 15), however the displacement thickness is about 1/3 of the boundary-layer thickness (coefficient 5 in the case of (i) and coefficient 1.721 in the case of (ii) type). To be on the safe side during the design process of the test sections, we used the first (i) type of the boundary-layer thickness, which we named as "velocity boundary layer thickness".

In some literature the velocity boundary layer thickness is named as a Blasius boundary layer. H. Blasius in 1908 solved the continuity and momentum equations by using the similarity solution using a power series expansion approach that solved the problem of laminar flow of a fluid over a flat plate (Cengel and Ghajar, 2015).

The velocity boundary layer thickness, denoted as δ_v, is defined as the thickness at the distance y, for which the following relation is true: $U_a = 0.99\, U_{a,b}$ (Schlichting and Gersten, 2016). Thermal and concentration boundary layers are defined similarly, with the following ratios: $\mathrm{abs}(T_w - T)/\mathrm{abs}(T_w - T_{a,b}) = 0.99$ and $\mathrm{abs}(C_{2,i} - C_2)/\mathrm{abs}(C_{2,i} - C_{2,b}) = 0.99$ (Bergman et al., 2011; Cengel and Ghajar, 2015). During the internal flow inside the tube or a non-circular duct, the velocity boundary layer develops with the increasing axial distance. The merging of boundary layer in the radial direction indicates the fully developed region. The same could be true for humid air flow between two vertical flat plates, if the plate's height is large or Reynolds number is low, considering the following equation describing the velocity boundary layer thickness of humid air (Schlichting and Gersten, 2016):

$$\delta_v = \frac{5L}{\sqrt{Re_{a,b}}} \quad \text{(Equation 15)}$$

L is the height of a vertical flat plate (L = 30–74 mm) and $Re_{a,b}$ is Reynolds number of the humid air flowing past the plate. The velocity boundary layer thickness is related to the thermal and concentration boundary layers of humid air by following relations:

$$\frac{\delta_v}{\delta_t} = Pr_{avg}^{1/3} \quad \text{(Equation 16)}$$

$$\frac{\delta_v}{\delta_C} = Sc_{avg}^{1/3} \quad \text{(Equation 17)}$$

Both Prandtl and Schmidt number are calculated temperature, defined as an average value between the plate's walls and the bulk flow temperatures, i.e. $T_{avg} = (T_{a,b} + T_w)/2$.

The designing process of all test sections considered four main variables (Figure S3): 1. humid air velocity over vertical flat plate ($U_{a,b}$), 2. vertical flat plate height (L) and 3. the distance between the isothermal side

walls and the first and last flat plate (d) and the distance between two neighboring plates (e). The analysis of the first two variables ($U_{a,b,}$ L) ensured laminar flow over the chosen geometry of all three test sections within the entire range of experimental variables (as shown in Chapter 1.2). Two remaining variables (d, e) were chosen based on the analysis of all three boundary layer thicknesses. We calculated all three boundary layer thicknesses (Figure S4) and compared with the chosen values d = 33 mm and e = 66 mm. As it turns out, the maximum value of the boundary layer thickness encompassing all experimental values has been obtained in the case of a concentration boundary layer with the value of δ_C = 7.4 mm (Figure S4). This value confirms the existence of the bulk flow, i.e. the free stream of the humid air, where the effects of velocity gradient, shear stress, temperature and concentration gradient inside all three boundary layers are negligible. The thickness of the bulk flow was in the range: $\delta_{a,b}$ = (d - 2·δ_C) up to (e −2·δ_C), i.e. $\delta_{a,b}$ = 18.2–51.2 mm. Thereby, in all the cases the following criteria was proven to be true: $\delta_C << \delta_{a,b}$. With this analysis we confirmed our choice related to the theoretical study of the condensation of water vapor in the presence of air on vertical flat plates.

Here we note that the boundary layer thickness plays a crucial parameter when designing the condenser in case of humid air flow past a series of vertical flat plates. Leading equations that define whether an external or internal flow must be considered are Equations 15–17. If the merging of two boundary layer exists between two flat plates forming a channel, then the flow must be treated as an internal flow.

Development of new semi-empirical correlation

Force balance. The correlation development was based on the conservation of mass, momentum and energy. The conservation of momentum is applied through the force balance, which gives us the following equations describing the liquid film velocity U_c of an element of condensate flowing along the y axis of a vertical flat plate (Faghri and Zhang, 2020):

$$U_c = \left(\frac{g\rho_c}{\mu_c}\right)\left(\delta y - \frac{y^2}{2}\right) + \frac{\tau_i}{\mu_c} y \qquad \text{(Equation 18)}$$

The condensate mass flow rate per unit width of surface is given by integration of Equation 18 with respect to y from 0 to δ (condensate thickness):

$$\Gamma = \rho_c \int_0^{\delta} U_c dy = \frac{g\rho_c^2\delta^3}{3\mu_c} + \frac{\tau_i\delta^2}{2\mu_c} \qquad \text{(Equation 19)}$$

Where ρ_c is condensate density considered as a constant, g is gravitational constant, δ is the condensate thickness and τ_i is the shear stress at the liquid-vapor interface. The detailed description of the derivation of the Equation 18 can be found in (Faghri and Zhang, 2020) for the case of laminar condensate flow over a vertical flat plate taking into account effects of vapor motion.

Heat balance at the interface. The conservation of energy is related to the heat balance at the interface during the condensation of the vapor on the vertical plate. It can be calculated by considering two contributions: heat conduction through the condensate film and the condensation at the liquid-gas interface. The basic equation for the derivation of the heat balance can be obtained by the following expression (Faghri and Zhang, 2020; Fujii, 1991):

$$\frac{\rho_c c_{p,c} \nu_c}{Pr_c}\frac{dT}{dy} = q_c'' = \mu_c h_{fg}\frac{d(\Gamma/\mu_c)}{dx} \qquad \text{(Equation 20)}$$

where $c_{p,c}$, ν_c, Pr_c are condensate's specific heat, kinematic viscosity and Prandtl number, respectively. q_c'' is condensation heat flux and h_{fg} is a latent heat of vaporization. First, due to its small variation, the dynamic viscosity of the condensate can be considered constant, which can be omitted from the derivation and canceled on the right-hand side of Equation 20. Next assumption is related to the temperature difference dT in the condensate, which can be treated as linear (Faghri and Zhang, 2020). The term dT/dt can be therefore expressed as (T_i - T_w)/δ. Knowing that the Prandtl number of the condensate can be expressed as ($\rho_c c_{p,c} \nu_c / k_c$), then the final equation related to the heat balance is in the form:

$$q_c'' = k_c\frac{T_i - T_w}{\delta} = h_{fg}\frac{d\Gamma}{dx} \qquad \text{(Equation 21)}$$

where k_c is thermal conductivity of the condensate.

Nusselt and Sherwood numbers. The problem of the fluid flow over the flat plate has been solved by Blasius using the similarity transformation (also known as Blasius solution). The similarity solution provides a mean to reduce the complex system of boundary layer partial differential equations into ordinary type of differential equations (Katopodes, 2018), which then lead to solutions for the wall shear stress (Equation 22), interface shear stress (Equation 23), and the Nusselt and Sherwood number (Equations 24 and 25), see also (Bergman et al., 2011; Cengel and Ghajar, 2015).

The shear stress on the wall using similarity transformation has been defined as:

$$\tau_w = 0.332 U_{a,b}^{3/2} \sqrt{\frac{\rho_{a,b}\mu_{a,b}}{x}} \quad \text{(Equation 22)}$$

At the liquid-bulk flow interface, the interface shear stress can be assumed as a wall shear stress in the case of flow over a thin flat plate. The Equation 22 can be further rearranged into the following form:

$$\tau_i = 0.332 Re_{a,b}^{3/2} \left(\frac{\mu_{a,b}^2}{\rho_{a,b} x^2} \right) \quad \text{(Equation 23)}$$

The Nusselt number in the case of the fluid flow over the flat plate is a well-known correlation, defined as:

$$Nu = 0.332 Re_{a,b}^{1/2} Pr^{1/3} \quad \text{(Equation 24)}$$

By considering the heat and mass transfer analogy, also knowing that the following functional relations is true: $Sh = (x^*, Re_{ab})\, Sc^n$ (Bergman et al., 2011), the analogy may be used to define the Sherwood number as:

$$Sh = 0.332 Re_{a,b}^{1/2} Sc^{1/3} \quad \text{(Equation 25)}$$

x^* is a dimensionless spatial coordinate, defined as: $x^* \equiv x/L$.

The account of the non-condensable gas. The account of the NCG is very important for the condensation process, as even a small amount of the NCG changes the transport mechanism of the condensation from the liquid-phase heat transfer controlled to the vapor-phase mass transfer controlled (Asano, 2006). Since the total pressure is constant inside the vapor boundary layer, the following equations describing the total pressures at the interface and in the bulk flow are: $p_{tot,i} = p_2(T_i) + p_1(T_i)$ and $p_{tot,b} = p_2(T_{a,b}) + p_1(T_{a,b})$. The combination of both equations yields $p_1(T_i) - p_1(T_{a,b}) = p_2(T_{a,b}) - p_1(T_i) > 0$, indicating the accumulation of a non-condensable gas (air) near the liquid-vapor interface. The accumulated air near the interface creates an additional thermal and mass resistance in the vapor phase.

In the case of the humid air condensation process, the rapid decrease of specific volume is observed due to water vapor condensation. This creates the so-called "suction effect" (Gross et al., 1961), denoting water vapor transport to the liquid-gas interface. The accumulated air near the interface hinders the suction force, reducing the temperature at the interface, also affecting not only thermal, but velocity and concentration boundary layers as well. The driving force of the vapor mass transfer can be defined by the mass fraction-difference ratio, which for the case of humid air condensation with respect to air can be defined as a factor Y (Stephan and Laesecke, 1980):

$$Y = \frac{W_{1,i} - W_{1,b}}{W_{1,i}} \quad \text{(Equation 26)}$$

$W_{1,i}$, $W_{1,b}$ are mass fractions of air in humid air at the liquid-gas interface and in the bulk flow, respectively.

In this study we considered a correlation that accounts the air as a non-condensable gas in the humid air flow. This has been theoretically analyzed in details by several authors (Asano, 2006; Fujii, 1991). Fujii (Fujii, 1991) proposed a correlation with an accuracy of $\pm 2\%$ accounting different binary mixtures: ethanol-water, R-114–R-11; air-water, air-ethanol, air–R-114; and air–R-22. The range of theoretical operating conditions was as follows: total pressure, p_{tot} = 0.05–0.8 MPa, $T_{dew,b}$ = 12–98.5°C, $W_{1,b}$ = 0.020–0.906. Here we note that listed correlation has not been experimentally confirmed by Fujii. Our initial comparison of theoretical and experimental condensate mass fluxes showed worse agreement in the case of air mass fraction in the bulk of humid air ($W_{1,b}$) higher than 0.9. Therefore, based upon our experimental and theoretical analysis we extended the applicable range of the correlation for higher air mass fractions in the bulk of

the humid air. The correlation that accounts the air inside the bulk of humid air with extended applicable range is defined as:

$$F = 0.91\left(\frac{2.5}{1.5+\frac{W_{1,i}}{W_{1,b}}}\right)^{m}\left(\frac{W_{1,i}-W_{1,b}}{W_{1,b}}\right)^{0.931} \quad \text{(Equation 27)}$$

The exponent m is expressed as follows (Fujii, 1991):

$$m = 0.425 + 0.050\ Sc_{a,V} + 0.011\ ln\ R \quad \text{(Equation 28)}$$

where $Sc_{a,V}$ is Schmidt number of humid air inside the vapor boundary layer and can be calculated using Equation 3, defined in the main text. Here the properties can be calculated at an average temperature between the interface and the bulk flow. Variable R is defined as the following ratio:

$$R = \left(\frac{\rho_c \mu_c}{\rho_V \mu_V}\right)^{0.5} \quad \text{(Equation 29)}$$

F function applicable range extension. Initial comparison between theoretical and experimental condensate mass fluxes showed worse agreement between theoretically and experimentally obtained condensate mass fluxes at air mass fraction inside the bulk of humid air above 0.9, as demonstrated in Figure S5 by the red shaded area. In comparison to the green shaded area, representing ratios with the air mass fractions below 0.8, the ratios in the red shaded area were significantly lower, in some cases coming close to 0.7. The prevailing observation regarding the performance of the presented correlation shows larger deviations in region with very large air mass fractions ($W_{1,b} > 0.9$), otherwise the correlation's results agree well with the experimental values.

The main reason for worse agreement in the case of larger air mass fractions is the applicable range of the Fujii correlation that accounts the non-condensable gases, as the correlation is valid for the non-condensable gas mass fraction in the bulk of different mixtures in the range $W_{1,b}$ = 0.020–0.906. Looking closely at the Tables 3.3-1 in Fujii (Fujii, 1991), the mass fraction of the air in the bulk of air-water mixture is $W_{1,b}$ = 0.0625–0.4068. Our study considered significantly higher air mass fractions, up to 0.974.

As the F function shows the functional dependence on the variable $\left(\frac{W_{1,i}}{W_{1,b}}-1\right)$, we have decided to extend the applicable range of the F function using the following equation:

$$F_{new} = \frac{F}{\beta\left(\frac{W_{1,i}}{W_{1,b}}-1\right)^{\varphi}} \quad \text{(Equation 30)}$$

Where F function is defined as:

$$F = \left(\frac{2.5}{1.5+\frac{W_{1,i}}{W_{1,b}}}\right)^{m}\left(\frac{W_{1,i}-W_{1,b}}{W_{1,b}}\right) \quad \text{(Equation 31)}$$

For the sake of simplicity the ratio of $W_{1,i}$ and $W_{1,b}$ can be defined as: $W_R = W_{1,i}/W_{1,b}$. Both constants, β and φ have been determined by plotting the ratio of the theoretical and experimental condensate mass fluxes in relation to (W_R-1) considering the height L = 50 mm of vertical plates. The data related to this height has been chosen, since we performed actual measurements of side wall's temperatures. This provides the most accurate analysis considering the extension of the applicable range of the F function. On the basis of the observed data from Figure S6 the values of (W_R-1) are generally between 0 and 0.4. The values closer to zero represent a region that is outside the applicable range of the Fujii's correlation. On the contrary, values closer to 0.4 indicate a region closer to the Fujii's applicable range and hence the plotted ratio approaches to 1. The data in Figure S6 has been fitted with the power function in the form of $\beta(W_R\text{-}1)^{\varphi}$. The first step was to obtain the value of φ, which has been calculated as the average value of all four values representing main and three parts of side walls: φ = (0.0692 + 0.0673 + 0.0662 + 0.0739)/4 = 0.0692. The value of β has been calculated as a solution to the problem, where we seek the value of the condensate mass flux ratio as close to 1 encompassing all experimental data. According to the β values of all four functions, the

solution of the final value of β will be within the range 1.09–1.20. The final value of β has been determined as 1.10. Final equation representing function F_{new} with extended applicable range is therefore:

$$F_{new} = \frac{F}{1.10(W_R - 1)^{0.0692}} \quad \text{(Equation 32)}$$

Condensation on test section's side walls

The test sections with vertical plates used in this study were made from the copper. As the low-resistance thermal contact between the hollow copper channels and side walls existed due to copper-to-copper contact (check Figure S3), the heat flow between side walls and channels was present as well. In order to comprehensively compare the predicted condensate mass flux values at different operating conditions, the condensation from the side walls had to be calculated. The influence of additional condensation on side walls was evaluated only for two sides, where the contact between the channels and side walls existed. Other two isothermal side walls with no contact between the channels and side walls were not considered.

The main unknown variable was the temperature of the side walls in contact with hollow copper channels in which cooling water flowed. Additional set of nine experiments has been performed for the test section with the plate's height of 50 mm. Besides typical values $T_{a,b}$, T_w, $\dot{V}_{a,b}$ and $m''_{avg,exp}$, the temperature of the half of the side wall was measured in 16 points [Figure S7A)]. The discrete values of these points along other measured values are shown in the Table 4 in (Poredoš et al., 2021a) for 9 different measurements, with the range of $T_{a,b}$ = 30.0–75.5°C, T_w = 20.9–58.6°C, $\dot{V}_{a,b}$ = 0.060–0.062 $m^3\ s^{-1}$ and $m''_{avg,exp}$ = 0.33–7.56 $g\ s^{-1}\ m^{-2}$.

Based on the observed temperatures [Table 4 in (Poredoš et al., 2021a)] it is clearly evident that condensation occurs on the side walls, as some parts of the side wall were at significantly lower temperatures compared to the humid air temperature at the inlet. The whole area of a side wall was divided into three main parts, indicated by three different colors [Figure S7B)]: first blue colored part indicates area between channels, second green colored part indicates area between the channel and the edge, and third yellow colored part indicates area above the channels. For each part the average temperatures $T_{side\text{-}w,1}$, $T_{side\text{-}w,2}$ and $T_{side\text{-}w,3}$ have been calculated based on the additional experiments. The Table S2 shows all the respectable equations used for the calculation of average temperatures for parts 1-3.

The average temperature of the first part was calculated as the average between the temperature, observed at the contact between the channels and side walls (T_{cont}) and the temperature, observed in the middle of two successive channels ($T_{side\text{-}w,mid}$). Both temperatures were determined as a function based on the experimental dataset (Figure S8), where temperature measurements with the respectable indexes are shown in the Table S2. The temperature defined by the index 17 has not been measured. Since the location of the measurement position 3 was inside the third part, average temperature with the index 17 at the border between part 1 and part 3 was calculated as an average temperature of indexes 3 and 8 and is highlighted with the gray circle, as depicted in Figure 5B). The average temperature of the second and third parts was calculated similarly to the first. The temperatures of the edge (T_{edge}) and upper side (T_{up}) were determined from functions based on the experimental data (Figure S8).

The analysis of the condensation process on side walls disregarded the condensation on side walls in the part 4. The majority of the condensation process occurs on vertical flat plates and side walls in parts 1-3 due to combined effect of higher temperature difference between the humid air and the wall temperature and, smaller film thickness and lower air mass fraction of humid air in these parts. Due to intensive condensation process in parts 1-3, larger film thickness on side walls in part 4 is presented along with lower temperature difference and with highly dehumidified humid air flowing across side walls in this part. The calculation of the condensate mass flux with the inclusion of the condensation on side walls on parts 1-3 has been done using the equation:

$$m''_{avg,th} = \frac{A_{main} m''_{avg,main} + A_{side-w,p1-2}\left(0.75\ m''_{avg,side-w,p1} + 0.25\ m''_{avg,side-w,p2}\right) + A_{side-w,p3} m''_{avg,side-w,p3}}{A_{main}}$$

(Equation 33)

where A_{main} = 0.152 m^2, 0.093 m^2 and 0.059 m^2 for L = 74 mm, 50 mm and 30 mm, respectively, $A_{side\text{-}w,p1\text{-}2}$ = 0.03915 m^2, 0.02645 m^2 and 0.01587 m^2 for L = 74 mm, 50 mm and 30 mm, respectively, $A_{side\text{-}w,p3}$ = 0.02722 m^2 (L = 50 mm).

In future experimental studies, superhydrophobic coating for anti-condensation properties of all four side walls will be considered, as recent progress in the domain of surface engineering for anti-condensation applications recently demonstrated promising results (Wu et al., 2021; Xu et al., 2021). We believe that the accuracy of the correlation could be further increased by such coating, also reducing the time and costs, associated with additional experiments.